Phase separation of thin-film polymer mixtures under in-plane electric fields

Chen-Hung Wang,[1] Peilong Chen,[1] and C.-Y. David Lu[2]
[1]*Department of Physics and Center for Complex Systems, National Central University, Chungli 320, Taiwan*
[2]*Department of Chemistry, National Taiwan University, Taipei 106, Taiwan*
(Received 28 March 2010; published 16 June 2010)

Phase-separation dynamics of polymer thin-film mixtures of polystyrene (PS) and poly(methyl methacrylate) (PMMA) are observed while an *in-plane* electric field is applied, instead of the out-of-plane fields usually employed previously. The phase separation is accompanied by the formation of PS dewetting holes at zero or weak fields. The dewetting velocity at 0.25 μm/min is a few times slower than that seen in regular bilayer dewetting. With the increasing of the field strength, we observe the formation of PS droplets in PMMA matrix, a reversal from zero- or low-field conditions. The PS dewetting holes are also suppressed. At further increased fields, PS droplets quickly penetrate up to the top of the PMMA matrix, leading to smaller and more irregular final PS droplets. This is manifested in the dramatic decrease in the growth exponent of the droplet size $\mathcal{L}$ from $\mathcal{L}\sim t^{1.5}$ to $\mathcal{L}\sim t^{0.1}$. These morphology changes are explained by the electrostatic energy resulted from the PS and PMMA dielectric contrast.

DOI: 10.1103/PhysRevE.81.061501 PACS number(s): 64.75.Va, 64.75.St, 77.55.−g

I. INTRODUCTION

Phase separation in thin-film geometry has been actively studied due to fundamental as well as application aspects. Further interests are generated by the possibility of using external fields, such as electric fields [1–7], to control the dynamics and morphology. However, almost all the previously used external fields are perpendicular to the thin films [2,3,5,6]. In this paper we report the results of polymer thin-film phase separation when in-plane electric fields are applied [4].

Homogeneous binary polymer mixtures undergo phase separation when quenched below the critical temperature. The phase morphology goes through various nonequilibrium patterns, which are typically classified as the spinodal decomposition (either bicontinuous or droplet) or nucleation growth. In a bulk system the average domain size $\mathcal{L}(t)$ typically grows as a power law of $\mathcal{L}\sim t^n$. In the early stage, the phase separation of a near-critical blend is governed by the diffusion [8], which gives $n\sim 1/3$. At the late stage, both hydrodynamics [9] and collision-induced-collision (CIC) [10,11] mechanisms for critical or near-critical blends yield a crossover from $n\sim 1/3$ to $n\sim 1$.

In thin-film experiments, interfaces of polymer/substrate and polymer/air could change phase-separation morphology dramatically. At the polymer/substrate interface, not only the surface directed spinodal decomposition (SDSD) [12] creates time-dependent density waves propagating perpendicular from the substrate into the bulk [13,14], but also a wetting layer forms on the substrate by the preferred species [15,16]. SDSD also changes the composition away from the polymer/substrate interface, making the final morphology different from those in the bulk. For thin samples confined between two solid surfaces, Tanaka [17] and Bodensohn and Goldburg [18] revealed that the wetting changes the growth of disklike droplets from power laws to logarithm. Domains may become channels between two wetting layers on the two solid surfaces, hence increasing the coupling between domains.

In most polymeric thin-film experiments, however, there is an open surface and early studies focus mainly on the final morphology [19–23], which is characterized by hill-like domains of one species embedded in the wetting layer of the other. This morphology may be resulted from the phase-separated domains dewetting on the wetting layer. However, few experiments have shown the pathways leading to such morphology. To our knowledge, Wang and Composto [24] were the first to study the dynamics of the dewetting pattern. They found that, in poly(styrene-ran-acrylonitrile) and poly(methyl methacrylate) (PMMA) systems, not only the wetting layer rapidly forms at the polymer/substrate interface by SDSD in the beginning, but also at the polymer/air interface. The wetting layers eventually thin when the middle layer reaches the late stage of phase separation, which makes hydrodynamics flows from the top to bottom layers through connecting domains possible. The capillary pressure due to the curvature of the cylindrical channels embedded inside the nonwetting matrix finally increases the channel size and ruptures the continuous matrix of the nonwetting component into dropletlike domains. This capillary pressure is also responsible for the roughness at the polymer/air surface at the beginning.

As for the polymer/polymer interface, it is known that an external force such as an applied electric field will induce interfacial instabilities [4,25–28] which produce stripe or columnar patterns in polymer thin films [5,28], polymer bilayers [6,29], block copolymer microphases [4,30], solvent-free spin-casting films [31], and polymer/liquid-crystal mixtures [32]. Onuki [33] pointed out that interface instability of immiscible nonionic liquids can be induced by an electric field applied perpendicular to the interface. The instability could eventually break the interface and orient them along the field direction. This effect decreases away from the electrode and increases with the dielectric constant contrast and the field strength. It is shown [29] that in polystyrene (PS) and PMMA bilayers (air/PS/PMMA/Si), an electric field perpendicular to the PS/PMMA interface enhances long-range instability and results in PS columnar dewetting domains onto the PMMA layer.

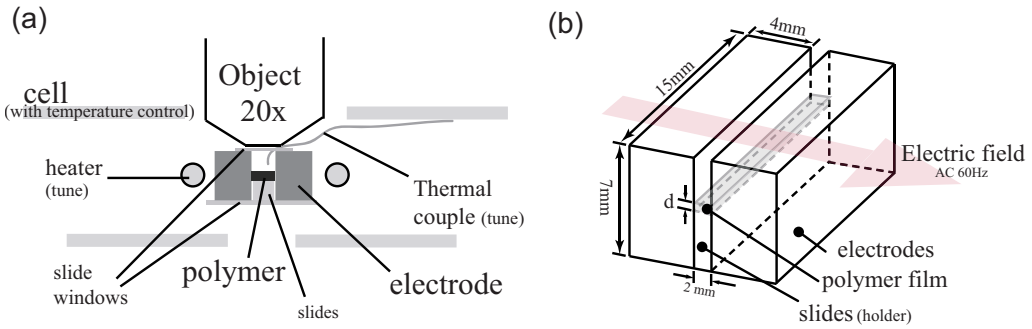

FIG. 1. (Color online) The sketch of the setup. (a) The side view of the setup (not in scale). The polymer thin film is placed in the middle of two metal electrodes and two slides are used as windows covering on the top and bottom of the electrodes. Beside the outer temperature control cell (only portions are shown), there is another set of (tune) thermal couple and heater nearby the electrodes to maintain the temperature fluctuation within ± 0.1 °C. The outer cell and object are all cover by Kapton tape and grounded with a high-voltage transformer which provides the electric field. (b) The detail geometry of the electrodes and the thin film. The film with slide substrate is held by slides at the center of the electrodes. The distance between electrodes is 2 mm.

In this paper, we describe results from experiments observing phase separation in polymer thin films of PS/PMMA mixtures with applied in-plane electric fields. By using thin-film phase-separating polymer mixtures, polymer/polymer interfaces will be created in the horizontal (lateral) direction rather than in the out-of-plane direction. Thus, in-plane electric fields will have much larger effects on the dipolar interaction of the lateral interfaces. At zero or weak field strengths, we recover usual droplet-type spinodal decomposition in our off-critical blends, with later morphology dominated by the formation of dewetting holes. Upon increasing the field strength, the effects of electrostatic energy significantly change morphology evolutions. Specifically over a critical strength, the external field reverses the composition of droplet formation from that determined by the asymmetrical spinodal curve alone (from PMMA to PS droplets). This reversal leads to completely different subsequent evolutions. Even stronger fields are further seen to quickly lift the droplets up to the film surface, yielding much smaller final length scale and irregular PS domains on top of the PMMA film.

II. EXPERIMENTAL SETUP

The thin films are prepared from off-critical [34] blends of PS (molecular weight=13 000 g/mol) and PMMA (15 000 g/mol) with a 50/50% weight ratio by spin casting from a 15% toluene solution onto freshly cleaned 2×2 cm^2 glass slides. The films are transparent, but under a microscope faint submicro-spinodal-type structures are seen, which may be the preseparated domains during the spin casting and solvent evaporation. After parts of the film are removed mechanically, an atomic force microscope (AFM) is used to measure the film thickness by scanning across the edge of the film. The film thickness we use is in the range of 0.5–2 μm. AFM images also reveal bumps sized about 1 μm high and 10 μm wide decorating on the coated film with an area fraction of about 3%, which may be the impurities or preseparated PMMA in solvent. The samples are then cut into 2×5 mm^2 strips and placed between two electrodes covered by the *Kapton* tape for electrical insulation as shown in Fig. 1.

Figure 1(a) shows the side view of the relative positions of the film, electrodes, and the objective lens. The temperature is controlled for the surrounding cell and also tuned by a set of heater and thermal couple adjacent to the electrodes. Both the cell and the object are electrically grounded and the sample is held to the center of the electrodes. The detail dimensions of electrodes are shown in Fig. 1(b). The spacing between electrodes is 2mm and an in-plane 60 Hz electric field E is used. The film placed between electrodes is preheated without applied electric field for 40 min at 110 °C to remove residential solvent. High-voltage transformers sharing the same ground are used as the source of the electric field. The temperature is then raised to 142.5 ± 0.1 °C, which is above the glass transition temperature but still below the phase-separation temperature at about 210 °C ($T/T_c \sim 0.875$). Once the temperature reaches the target value, an electric field is applied with the field strength adjustable between 0 and 1 V/μm.

The uniformity of the electric field is checked by the homogeneity of the morphology at every field strength. Up to $E=0.6$ V/μm, the film is homogeneous between the electrodes (2 mm in width) and in longitudinal direction (at least 5 mm in length). At higher field strength, within 50 μm of the edge of the film, the morphology is slightly different with those in the middle. The ratio of this region to the system size is about 5%.

The evolutions of morphology are recorded by an optical microscope. The annealing time ranges between 12 and 140 h. Afterward, the samples are cooled down to the room temperature and the surface profiles of the final morphologies are measured by an AFM both before and after immersion into selective solvents, cyclohexane or acetic acid, to identify PS or PMMA domains. The AFM identification together with optical images provides enough information to infer the pathways of final morphology formation and the effects of the electric field.

III. RESULTS AND DISCUSSIONS

We will concentrate our discussions on the morphology evolution of 1.6-μm-thick films under increasing strength of

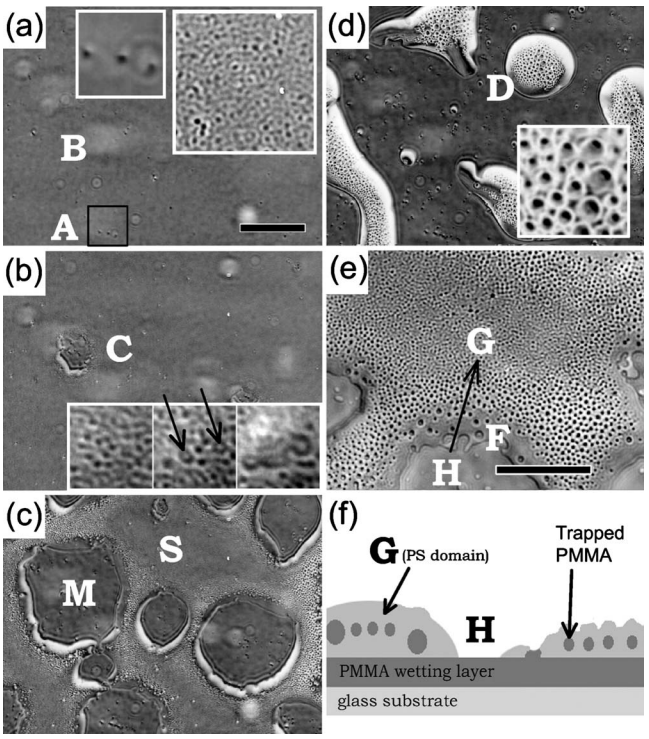

FIG. 2. A typical evolution of a 1.6-μm-thick film undergoing phase separation at $E=0$. The times are (a) 10 min, (b) 31 h, (c) 63 h, and (d) 131 h. (e) is a typical morphology near dewetting holes at 500 min in another sample, and (f) is an illustration of the side view of (e). The small inset of (a) and the inset of (d) with widths 50 μm are enlargements of area A and the center of the puddle D, respectively. The larger inset in (a) is the initial spinodal pattern and the width of the inset is 60 μm. The inset in (b) with a whole width of 60 μm and time intervals of 30 min is the time series of larger trapped PMMA droplets breaking the PS film. (a)–(d) are in the same scale and the scalar bar is 150 μm. The scale bar in (e) is 60 μm.

electric fields. It is found that the evolution can be categorized into three distinct regions of the field strength.

A. Weak-field regime

Figure 2 in which $E=0$ demonstrates a typical evolution of 1.6-μm-thick films undergoing phase separation while $E<0.6$ V/μm. The film surface is decorated with hill-like structures prior to annealing. In the left inset of Fig. 2(a), the enlargement of area A shows three such bumps. In thinner films ($\sim$800 nm) these bumps have similar sizes, indicating their origins as material impurity. The area marked B appears to be imaging noises as they remain unchanged with time or on moving the sample.

At the beginning of annealing, a PMMA wetting layer forms on the slide surface, and away from the substrate inside the film there is a faint PS/PMMA bicontinuous network increasing its contrast and coarsening in the first 30 min of annealing, shown in the larger inset of Fig. 2(a). After 1–2 h of annealing, droplets will gradually form [see the insets of Fig. 2(b)] which later on could initiate the formation of dewetting holes [marked C in Fig. 2(b)]. These patterns are consistent with an off-critical blend undergoing droplet-type spinodal decomposition, which has a network domain at the beginning of phase separation and then turns into droplets.

After the initial formation of PMMA droplets from the networklike structures, the droplets coarsen at a significantly slower rate. Since the coarsening develops by molecular diffusion (we see no evidence of hydrodynamics at this stage), once droplets formed, the diffusion of PMMA molecules across separated droplets should slow down with a factor on the order of $\exp(\Delta F/k_BT)$, with ΔF as the energy barrier due to the PS matrix. ΔF can be estimated from the Flory-Huggins parameter $\chi\approx 0.034$ [35] for PS/PMMA and the monomer number of PMMA being about 150 in our sample (thus, $\Delta F/k_BT\approx 0.034\times 150\approx 5$). This leads to a slowing factor of about 150, consistent with what is observed (from minutes to hours or tens of hours) [36]. At $\sim$20 h of annealing, the film starts breaking and is featured by the dewetting holes as marked C in Fig. 2(b). The dewetting holes are mostly initiated at larger PMMA droplets as observed in the inset of Fig. 2(b). The time series images in the inset indicate that PMMA droplets with sizes similar to the film thickness (marked by arrows) can connect to and then are absorbed by the PMMA wetting layer. This opens a hole on the metastable PS film.

The dewetting holes grow and gradually connect to each other as in Fig. 2(c). However, the PS matrix marked by S still contains many trapped PMMA droplets. Selective solvent erosion did show that the bottom of the dewetting holes, marked as M in Fig. 2(c), is a wetting layer of PMMA on the glass substrate. Eventually the domains shrink into puddles on the PMMA wetting layer and reach a height of about 5 μm, as marked by D in Fig. 2(d). The inset of Fig. 2(d) shows the interior of region D, containing trapped PMMA droplets.

During dewetting, the trapped PMMA droplets near the receding contact line will coarsen or re-enter the PMMA wetting layer. Figure 2(e) shows the area near a dewetting hole after 500 min annealing in another sample. The dewetting hole (light gray area marked by H) is surrounded by the dewetted PS matrix (deep gray area G) which contains many PMMA droplets. They are separated by the contact line F. When the contact line moves as indicated by the arrow, the PMMA droplets near the contact lines are pushed toward the interior of the PS matrix and would merge with droplets further inside. Thus, in general droplets near the contact line are larger.

The irregular shape of the contact line F is quite different from the smooth contact lines usually seen in the solid-liquid [37] or liquid-liquid [38] dewetting. AFM data reveal that the circles next to the contact line F are concave holes and those further away are convex droplets indicating that the trapped PMMA droplets near the contact lines are absorbed down to the wetting PMMA layer. Subsequently, the circumference of those droplets will become part of the contact line, leading to the irregular shape.

The side view of the final morphology is illustrated in Fig. 2(f). At the late stage, a PMMA wetting layer forms on the substrate with partially dewetted PS domains on top. Inside the PS domains, there are separated PMMA droplets. This final geometry is very similar to the wetting-induced double

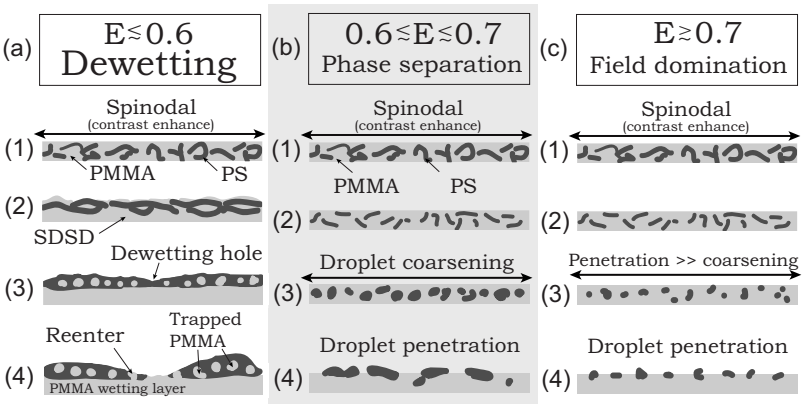

FIG. 3. Illustration of pathways to final morphologies at different electric fields.

separation in deep quench [39] where the secondary separation happens inside the main separated domains. Although the morphologies are both featured by droplets inside the heterologous domains, the scenarios are different. The trapped PMMA droplets are from the primary bicontinuous network and form before the dewetting of PS domains starts. Finally, the complete morphology evolution is summarized in Fig. 3(a).

The growth of the dewetting holes is shown in Fig. 4. The radii increase mostly linearly with time with an averaged dewetting velocity at 0.25 μm/min. The dewetting velocities under 0 and 0.2 V/μm are almost the same, indicating that the dewetting is determined mainly by the surface energies and viscosities of PS and PMMA.

Lambooy *et al.* [38] examined bilayer liquid-liquid dewetting of a PS thin film on top of a PMMA one (~100 nm for both layers) at 170 °C. They found that the radii of dewetting holes also increase linearly with time at $V=0.8$ μm/min for $M_{w,PS}=31\,000$ and $M_{w,PM}=95\,000$. Since the viscosity of PMMA is much larger than that of PS while they have similar molecular weights [40], these observations are consistent with the prediction of a fixed dewetting speed, [41]

$$V \sim \frac{\theta_E^3}{\eta_{PS}}, \tag{1}$$

for a liquid on a solid substrate, where θ_E is the equilibrium contact angle and η_{PS} is the viscosity of the PS film. The lower dewetting velocity of our films may be due to the lower temperature and the existence of trapped PMMA droplets inside the PS film, leading to the increase in the effective η_{PS}. We simply estimate the deviation of η_{PS} by treating these PMMA droplets as hard spheres inside PS matrix, i.e., a colloidal suspension. The effective η_{PS} then might be estimated by [42,43]

$$\eta_{PS}(\phi) = \eta_0\left(1+\tfrac{5}{2}\phi+5.9\phi^2\right). \tag{2}$$

With an area fraction $\phi_{PMMA}\sim 0.35$, $\eta_{PS}(\phi)/\eta_0 \sim 2.5$. The ratio is close to the reduction in the dewetting speed from 0.8 to 0.25 μm/min. However, we need to note that these two systems are quite different in film thickness (100 nm vs 2 μm), temperature (440 K vs 420 K), and dynamics (bilayer vs phase separation). In addition Eq. (2) is only a rough estimate. Thus, the quantitative agreement may just be a coincident.

The fact that the dewetting velocities under 0 and 0.2 V/μm are almost the same indicates that the influence of the in-plane electric field to the dewetting speed might not be important. The dewetting is still determined mainly by the surface energies and viscosities of PS and PMMA.

Figure 4 also shows that the dewetting velocity drops significantly at the late stage; at that time the dewetting rims approach each other. These could significantly change the film thickness and the dynamic contact angle, and thus affect the dewetting velocity.

B. Intermediate field strength

The dewetting of PS on PMMA persists until a critical field strength $E_L \approx 0.6$ V/μm is reached. Initial evolutions below and above E_L are similar—small (~1 μm) blurred binary networks as shown in Fig. 5(a) increasing their contrast after a few minutes of annealing. The most conspicuous feature in Fig. 5(a) is the small (~1 μm) dropletlike do-

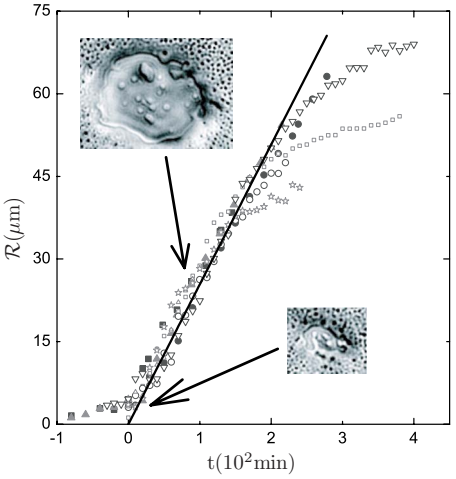

FIG. 4. (Color online) The effective radius R increases linearly with time for holes at $E=0$ V/μm (hollow) and 0.2 V/μm (solid). Times for different data sets are shifted to overlap. The solid line is the fitting of data between 0 and 150 min. The average dewetting velocity is 0.25 μm/min. The two insets with the same scale are the corresponding images of the holes.

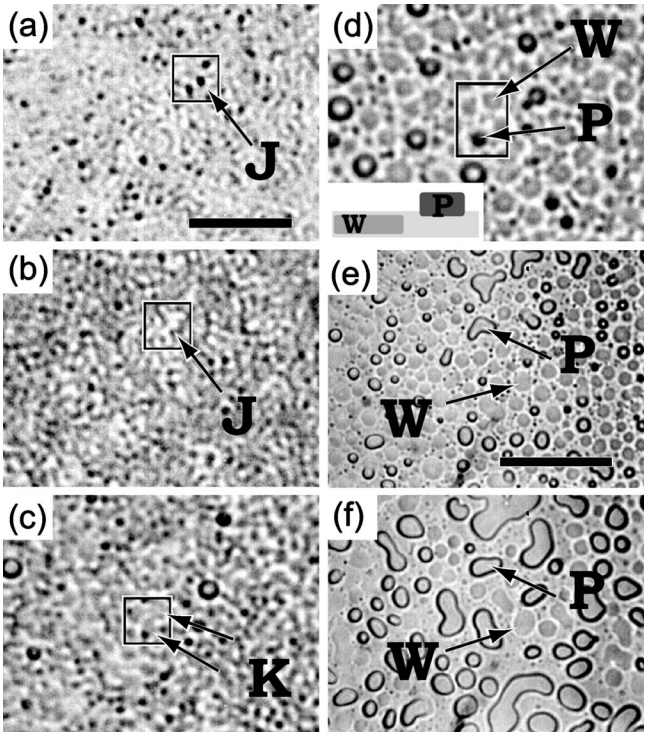

FIG. 5. Phase-separation evolution of a 1.6-μm-thick sample with an applied electric field at $E=0.62$ V/μm. The field is in the left-right direction, and parallel to the paper. The times are (a) 5, (b) 100, (c) 300, (d) 430, (e) 630, and (f) 1000 min. (a)–(d) are in the same scale with the scalar bar in (a) being 20 μm. Similarly for (e) and (f) with the 50 μm scale bar.

mains marked by J. These domains will be absorbed into darker network after ~1 h of annealing, with a time sequence illustrated in Fig. 6. From subsequent images and selective solvent tests, these dropletlike domains are PS. After 2 h of annealing, the film became featureless networks [Fig. 5(b)].

The PS network then iteratively breaks and reconnects while PS concentration gradient was built. Finally, ~5 μm PS droplets form after ~5 h [Fig. 5(c)]. Such PS pancakelike droplets marked by K will keep absorbing residual network. Meanwhile, the mobility of PS droplets increases and the droplets can grow by merging with another one or by CIC (Fig. 7) [10]. The increased mobility of PS droplets is likely due to hydrodynamics which originate from the force exerted by the electric field on polarization charges.

There are two kinds of PS droplets *W* and *P* in Fig. 5(d). The difference, as shown in the inset of Fig. 5(d), is that *W* is

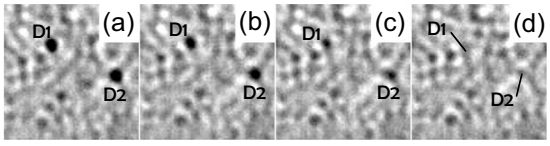

FIG. 6. Detail sequences of (PS) droplets marked by J in Fig. 5(a) being absorbed into the bicontinuous network. Droplets such as D_1 and D_2 become smaller and smaller and finally merge into the network as indicated at the last image. The width of each image is 20 μm and the time intervals between successive images are 10 min.

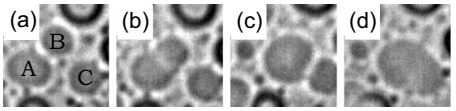

FIG. 7. PS droplets can coarsen through the collision-induced-collision (CIC) mechanism: the flow generated by the collision of droplets A and B induces the secondary collision of the nearby droplet C. The elapsed times between successive images are 30, 80, and 40 min. The width of each image is 10 μm and E is 0.62 V/μm.

inside but *P* is at the surface of the PMMA matrix. During further annealing, while *W*'s are colliding and merging with each other, they will contact with the bottom of *P*, being absorbed, and hence increase the size of *P* [Figs. 5(e) and 5(f)]. Figure 8 shows the sequence of two pancakelike domains *W* being absorbed by a droplet *P*. With its increased size, domain *P* seems immobile and is almost static on the top of the PMMA matrix even after ~20 h of annealing as in Fig. 5(f).

The first change in the morphology with $E \geq E_L$ is that dewetting holes no longer appear. The second is that the PS forms droplets, instead of forming PMMA droplets at small E. Of course it is very likely that the first is the direct consequence of the second. Comparing the inset of Fig. 2(b) and Fig. 5(c) we conclude that when the initial phase-separated binary network transfers into droplet structures, the high electric field induces the formation of PS droplets. It is noted that the eventual apparent area fraction between PS and PMMA actually remains about the same at $A_{PS}:A_{PMMA}$ ~0.65:0.35 for both below and above E_L. So what are the mechanisms with which the electric field induces the formation of PS droplets even when PS has a larger final apparent area fraction?

The external electric field can shift T_c [1,44–47]. This shifting could affect the phase-separation morphology since the spinodal line is asymmetric [34]. Large shift of T_c ~50 °C has be achieved in polymer blends at a field strength of about 30 V/μm [44]. However, this effect depends on the square of field strength. For the maximum field strength we used, 1 V/μm; the shift of T_c should be expected to be on the order of $10^{-3} \times 50$ °C=0.05 °C, which should not yield significant morphology change. Moreover, the area fraction close to E_L at which the morphology transition happens shows little change.

PMMA samples usually contain resident mobile ions, i.e., Li^+, from synthesis and these ions are selectively soluble in PMMA rather than in PS. When external electric field is applied, the ions can be polarized in PMMA domains and

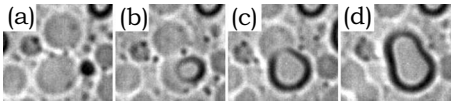

FIG. 8. These images demonstrate the initial penetration of a PS droplet in (b) and (c), and how another embedded droplet is subsequently absorbed by the first droplet in (d). The elapsed times between successive images are 80, 60, and 70 min. The width of each image is 10 μm and the field strength is $E=0.62$ V/μm.

introduce dipole-dipole and dipole-field interaction. In PS-PMMA diblock copolymers, it is shown that these ions can dramatically reduce the needed electric field strength for microstructure transition [7].

To quantify the effect of these ions, first we need an estimate of the amount of the ions. We take the ion density of $10^{10}/\mathrm{m}^3$ from [7] as the order of magnitude of the intrinsic ions' density. Under field strength $E_L=0.6\ \mathrm{V}/\mu\mathrm{m}$ and PMMA (volume fraction=0.6) as the matrix, if these ions Q completely separate to $d=2$ mm, the system size to form the dipole Qd, the energy density contributed from these ions is about $10^{-3}\ \mathrm{mJ}/\mathrm{m}^3$. On the other hand, the electrostatic energy density from dielectric contrast as calculated below can be estimated on the order of $\bar{\epsilon}E^2 \sim 10^4\ \mathrm{mJ}/\mathrm{m}^3$ with $\bar{\epsilon}=4$ as the average of ϵ_{PMMA} and ϵ_{PS}. Thus, it seems that, without additional ions, the effect of intrinsic ions is a minimal one.

Experiments on poly(2-chlorostyrene)/poly(vinyl methyl ether) [P2CS/PVME] blend [28], with similar field strength with ours, also suggest this is indeed the case. In [28], there is no significant anisotropy of phase-separation morphology until as high as 0.5 wt % of salt was added. If the free ions are the dominant mechanism, it is expected that some anisotropy will be present on the morphologies, which is lacking in this experiment.

External field could also induce dipolar interaction. At strong fields, e.g., 20 times larger than E_L [33], it is known that the dipolar interaction will produce anisotropic PS/PMMA interfaces [4,5,33]. However, with the small field strength and dielectric difference as in our system, these anisotropic patterns are not seen.

However, different dielectric constants for PS ($\epsilon_{\mathrm{PS}}=3$) and PMMA ($\epsilon_{\mathrm{PMMA}}=5$) will still yield different electrostatic energies under different configurations of droplets and matrices. Especially for phase separation in a thin-film geometry where the interfaces are mostly in the lateral direction, an in-plane electric field, whose field lines are running inside and parallel to the thin film, will have a much larger effect on the morphology than a perpendicular one. In electrostatics, the field lines prefer to concentrate on high-ϵ region. Thus, for argument's sake, consider the extreme case in which a two-dimensional system populated by two kinds of domains with vastly different ϵ's: $\epsilon_1 \gg \epsilon_2$ under a fixed area fraction. If due to kinetic constraint the domains are reaching only a certain length scale, it is more favorable for domains with ϵ_2 forming isolated regions while those with ϵ_1 forming a continuous matrix. In such configuration, the electric field lines can completely avoid ϵ_2 domains and run inside the ϵ_1 domains.

To get an estimate of the electrostatic energy in our system under this picture, we consider a simple droplet geometry as shown in Fig. 9(a). The light gray circles represent the droplets embedded in the dark gray matrix. Two configurations corresponding to PS and PMMA being droplets under applied in-plane electric field are used to mimic the two configurations for $E<E_L$ and $E\sim E_L$.

Unlike the usual formulation in the weak segregation of copolymer [1,30,48] or phase-separation systems [33], in which the free energy F is written as a functional of local composition distribution and proportional to $\Delta\epsilon^2$, we solve the Laplace equation for two cases with ϵ_{PMMA} either inside or outside the droplets in Fig. 9(a). The electric potential $\phi(x,y)$ under a uniform extend field E_0 is calculated by solving $\nabla[\epsilon(x,y)\nabla\phi]=0$, with $\phi \equiv -E_0 x+\phi^*$ and ϕ^* being periodic in x and y directions. The dielectric function $\epsilon(x,y)$ is spatially dependent reflecting the PS/PMMA distribution in Fig. 9(a). For this given configuration, the field line distribution only depends on the ratio $\epsilon_{\mathrm{in}}/\epsilon_{\mathrm{out}}$ rather than their difference. The system is then solved numerically using the finite difference method. The electrostatic energy is calculated with $\epsilon_1=3$ (ϵ_{PS}) and $\epsilon_2=5$ (ϵ_{PMMA}) as in Fig. 9(a) for one case, and ϵ_1 and ϵ_2 switched for the other. The results are plotted with equal potential contours in Figs. 9(b) and 9(c). Indeed we find that the total electrostatic energy for PS as droplets is lower by about 0.5%, compared to the configuration with PMMA droplets. The absolute magnitude of this energy difference ΔF_{elec} with $\epsilon_2=5$, $\epsilon_1=3$, $E_0=0.6\ \mathrm{V}/\mu\mathrm{m}$, and a droplet diameter of 5 μm is $\Delta F_{\mathrm{elec}} \sim 83\ \mathrm{mJ}/\mathrm{m}^3$, which is proportional to E^2.

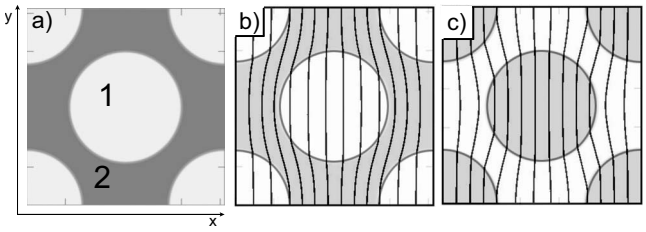

FIG. 9. Simple calculations of electric energy with dielectric contrast. The electric field $E_0=0.6\ \mathrm{V}/\mu\mathrm{m}$ is applied in x direction with potential $\phi \equiv E_0 x+\phi^*$, where ϕ^* is periodic in x and y directions. (a) The droplets (light gray) with a diameter of 5 μm and matrix (dark gray) configuration with equal area fraction and sharp interfaces. The dielectric constants are ϵ_1 for droplets and ϵ_2 for matrix (see text). (b) The contour lines of equal potential ϕ with $\epsilon_1=5$ (ϵ_{PMMA}) and $\epsilon_2=3$ (ϵ_{PS}). (c) The same as (b) but with ϵ_1 and ϵ_2 switched.

Now it may be tempting to compare this ΔF_{elec} to the surface energy difference between two well-developed droplet configurations [c.f. Fig. 5(e)], $\Delta F_{\mathrm{surface}}=F(\mathrm{PS\ droplets})-F(\mathrm{PMMA\ droplets})$, which could be quite large considering the final PS volume fraction being about 0.65. However, since the electric field is always acting on the film when the phase separation is developing [c.f. Fig. 5(b)], the energy difference ΔF_{elec} only needs to affect the initial stage when droplets just form from the bicontinuous networks. At this stage the two phases have very similar volume fractions with which the surface energy difference in forming either type of droplets should be much lower.

Thus, the electrostatic energy could drive the initial formation (from network) of PS domains into droplets instead of PMMA domains. Since the dewetting PS matrix at the lower field strength now becomes droplets, the PS dewetting hole morphology turns into PS droplets dewetting onto the top of PMMA matrix. During further annealing, the embedded pancakelike PS droplet W is lifted onto the polymer/air surface as shown in Fig. 5(f). A detailed sequence is also shown in Fig. 8. The floating PS island P has less mobility than the embedded PS droplet W, but still can increase its size by absorbing other embedded PS domains.

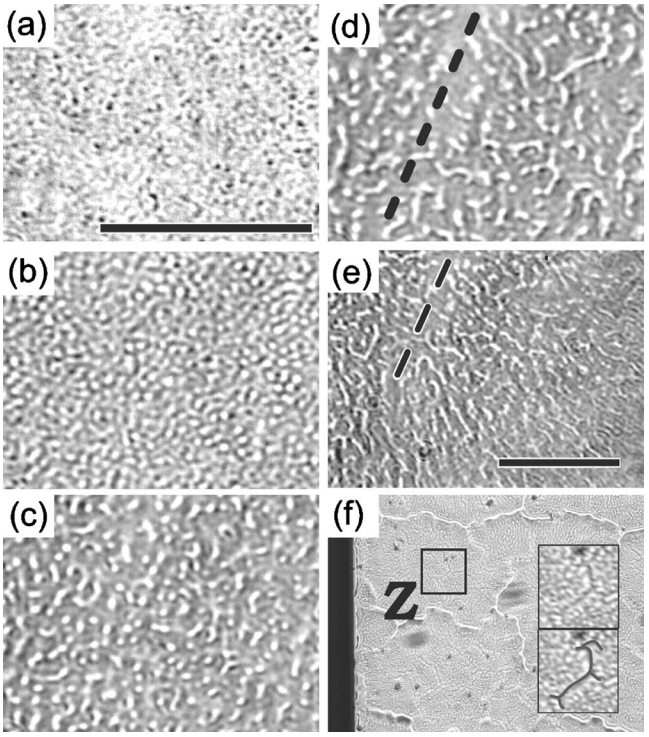

FIG. 10. Phase-separation evolution of a 1.6-μm-thick sample with an applied electric field at $E=0.9$ V/μm. The field is in the left-right direction and parallel to the paper. The times are (a) 20, (b) 51, (c) 300, (d) 550, and (e) 1000 min. (f) shows the large-scale crack of the film. The black rectangle on the left side of (f) is the electrode. The insets in (f) are the enlargement and the sketch of one subcrack of the area marked by Z in (f). (a)–(d) are in the same scale with the scalar bar at 50 μm in (a). The scale bar in (e) is 50 μm. The width of (f) is about 1 mm.

Eventually, the final morphology contains PS islandsfloating on the PMMA matrix as in Fig. 5(f). An illustration of morphology evolution at $E \sim E_L$ is also given in Fig. 3(b).

C. Strong field strength

Figure 10 shows a typical evolution as the field is further increased to 0.9 V/μm. In Figs. 10(a) and 10(b), the evolution of morphology is similar to Figs. 5(a) and 5(b), but after that the continuous PS network domain (light gray) breaks into small pieces and they quickly penetrate onto the surface of the PMMA matrix (dark gray), instead of coarsening to form droplets. These PS domains are immobile once on top of the PMMA layer, and the final domain sizes $\mathcal{L}^*$ are mostly determined at the stage [Fig. 10(c)]. Another notable change in morphology is that the irregularity of PS domains increases with the field strength. Illustration of the morphology evolution is shown in Fig. 3(c).

So the strong fields produce another effect which pushes the PS droplets up to the film surface quickly after they formed. The effect can also be explained by the dielectric contrast, such that by lifting the PS droplets out of the PMMA film, the electric field lines can concentrate and run more smoothly inside the higher dielectric domain of

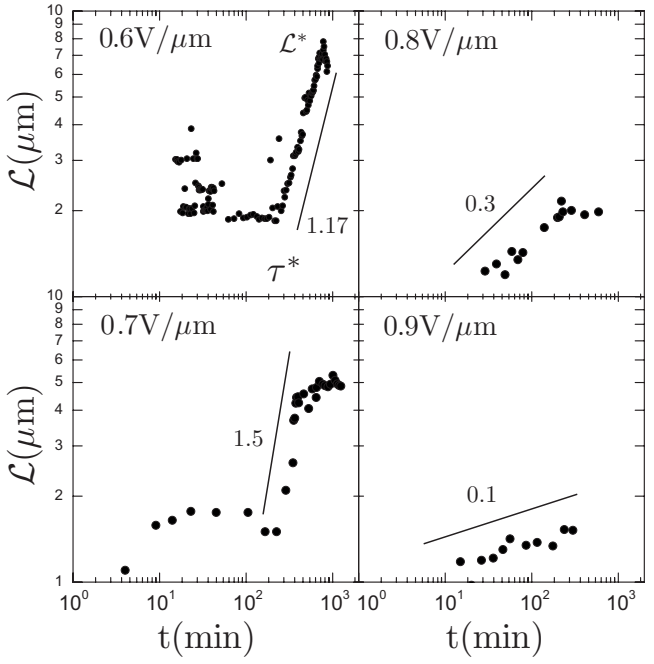

FIG. 11. The temporal changes of domain sizes $\mathcal{L}$ under different field strengths. The slopes of solid guide lines (growth rate exponents) decrease significantly from $E=0.7$ to 0.8 V/μm. The marker τ^* demonstrates the definition of the time that domains start coarsening and $\mathcal{L}^*$ is the final domain size.

PMMA. On top of the PMMA film, these small PS droplets then connect into irregular shapes.

After 500 min of annealing, the film starts cracking as indicated by the dashed line in Fig. 10(d). The cracking without preferred direction will stretch the PS domains to be longer and thinner, and most of them tend to direct perpendicular to the cracks as seen in Fig. 10(e) due to the stress, not due to the field. This alignment to the stress of crack will propagate into the film unless it meets another crack. A large-scale ($\sim$1 mm) cracking pattern is shown in Fig. 10(f), decorated with subcracks Z on the whole sample. The insets in Fig. 10(f) are the enlargement and the sketch of one subcrack in Fig. 10(f) marked by Z.

To study the dependence of typical domain sizes $\mathcal{L}$ on the field strength, we estimate $\mathcal{L}$ from the peak of the polar average of the two-dimensional Fourier transform of the microscope images before the PS domains have been pushed onto the top of PMMA (for $E \sim E_L$) or the formation of cracks (for $E > E_R$). There is no significant anisotropy between the directions parallel or perpendicular to the electric field. The time evolution of $\mathcal{L}$ under different electric field strengths is shown Fig. 11. The growth rates for $E_L = 0.6$ V/μm and $E_R = 0.7$ V/μm are much larger than those for $E=0.8$ and 0.9 V/μm. This dramatic switch can also be found in the time τ^*, defined as the time that domain coarsening takes place. It is remarkable that τ^* has a big jump for $E=0.7$–0.8 V/μm as seen in Fig. 12. Both Figs. 11 and 12 indicate another critical field strength E_R somewhere between 0.7 and 0.8 V/μm. As discussed earlier, this might be the field strength threshold after which the electrostatic energy induces separation in the direction perpendicular to the

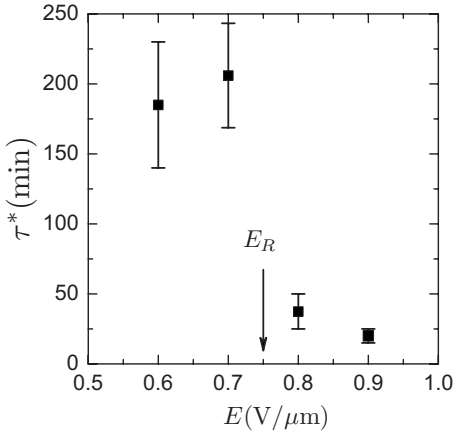

FIG. 12. The time τ^* at different electric fields E.

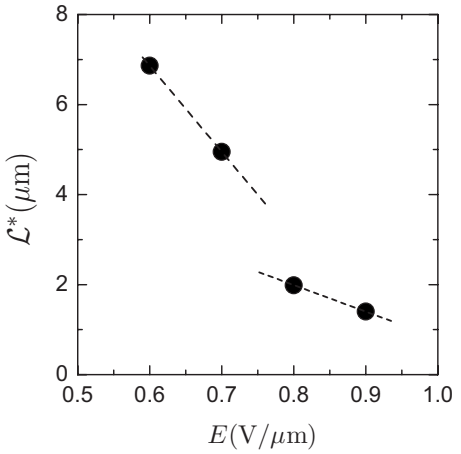

FIG. 13. The final domain sizes $\mathcal{L}^*$ at different electric fields E.

film. Within each field range $E_L < E < E_R$ and $E > E_R$, τ^* does not change with the electric field significantly.

Figure 13 is the measurement of the final domain size $\mathcal{L}^*$, which is decreasing with the increase in the field strength. $\mathcal{L}^*$ again follows two distinct trends before and after E_R. Finally, the complete morphology evolution is summarized in Fig. 3(c).

IV. SUMMARY

In summary, we observe that the in-film external electric field induces significant change in morphology evolution in quenched PS/PMMA thin-film mixture:

(1) At zero or weak field strengths, as the mixture has an asymmetric spinodal curve with PS-rich domains having a larger volume fraction, PMMA evolves into droplets inside continuous PS film which resides on top of a thin PMMA wetting layer on glass substrate. As PMMA droplets gradually grow due to diffusion, some of them eventually merge with the wetting layer. This then induces the formation of PS dewetting holes and breakup of the PS film, leading eventually to separated PS domains which still contain many small PMMA droplets.

(2) At intermediate field strength as the field effect becomes significant, we see the reversal of the droplet composition to the formation of PS droplets, against the preference set by the asymmetric spinodal curve. We believe that this is due to the dielectric contrast between PS and PMMA. With a higher dielectric constant, PMMA forms a continuous matrix to yield a lower electrostatic energy with in-plane field lines. The polarization due to the dielectric contrast also induces hydrodynamic motions, leading to fast collision and merging of PS droplets. Eventually the enlarged PS droplets penetrate onto the top of PMMA.

(3) With further increase in field strength, the PS droplets penetrate onto the top much earlier, where they become immobile without the aid of hydrodynamics. This fast up-penetration is likely the result of the strong field lines, which prefer to have a uniform distribution within the higher dielectric constant PMMA media. Consequently much smaller final PS droplets are seen. Later on the system also develops large millimeter-scale cracks, whose origin is still a mystery.

ACKNOWLEDGMENT

The support of the National Science Council of Taiwan is acknowledged.

[1] Y. Tsori, Rev. Mod. Phys. **81**, 1471 (2009).
[2] M. D. Dickey, S. Gupta, K. Amanda Leach, E. Collister, C. G. Willson, and T. P. Russell, Langmuir **22**, 4315 (2006).
[3] K. A. Leach, S. Gupta, M. D. Dickey, C. G. Willson, and T. P. Russell, Chaos **15**, 047506 (2005).
[4] K. Amundson, E. Helfand, D. D. Davis, X. Qian, S. S. Patel, and S. D. Smith, Macromolecules **24**, 6546 (1991).
[5] E. Schäffer, T. Thurn-Albrecht, T. P. Russell, and U. Steiner, Nature (London) **403**, 874 (2000).
[6] Z. Lin, T. Kerle, T. P. Russell, E. Schäffer, and U. Steiner, Macromolecules **35**, 6255 (2002).
[7] Y. Tsori, F. Tournilhac, and L. Leibler, Nature (London) **430**, 544 (2004); Y. Tsori, F. Tournilhac, D. Andelman, and L. Leibler, Phys. Rev. Lett. **90**, 145504 (2003).
[8] C. Domb and J. L. Lebowitz, *Phase Transitions and Critical Phenomena* (Academic Press, London, 1983), Vol. 8.
[9] E. D. Siggia, Phys. Rev. A **20**, 595 (1979).
[10] H. Tanaka, Phys. Rev. Lett. **72**, 1702 (1994).
[11] V. S. Nikolayev, D. Beysens, and P. Guenoun, Phys. Rev. Lett. **76**, 3144 (1996).
[12] S. Puri, J. Phys.: Condens. Matter **17**, R101 (2005).
[13] R. A. L. Jones, L. J. Norton, E. J. Kramer, F. S. Bates, and P. Wiltzius, Phys. Rev. Lett. **66**, 1326 (1991).
[14] G. Krausch, C.-A. Dai, E. J. Kramer, and F. S. Bates, Phys. Rev. Lett. **71**, 3669 (1993).
[15] S. Puri and K. Binder, Phys. Rev. E **66**, 061602 (2002).

[16] L.-T. Yan and X.-M. Xie, J. Chem. Phys. **126**, 064908 (2007).
[17] H. Tanaka, Phys. Rev. Lett. **70**, 2770 (1993).
[18] J. Bodensohn and W. I. Goldburg, Phys. Rev. A **46**, 5084 (1992).
[19] A. Karim, T. M. Slawecki, S. K. Kumar, J. F. Douglas, S. K. Satija, C. C. Han, T. P. Russell, Y. Liu, R. Overney, J. Sokolov, and M. H. Rafailovich, Macromolecules **31**, 857 (1998).
[20] X. Rui, Z. Song, S. Jing, and T. Decheng, Polym. J. (Tokyo, Jpn.) **37**, 560 (2005).
[21] M. Harris, G. Appel, and H. Ade, Macromolecules **36**, 3307 (2003).
[22] C. Ton-That, A. G. Shard, R. Daley, and R. H. Bradley, Macromolecules **33**, 8453 (2000).
[23] Y. Li, Y. Yang, F. Yu, and L. Dong, J. Polym. Sci., Part B: Polym. Phys. **44**, 9 (2006).
[24] H. Wang and R. J. Composto, J. Chem. Phys. **113**, 10386 (2000); Interface Sci. **11**, 237 (2003).
[25] J. M. Reynolds, Phys. Fluids **8**, 161 (1965).
[26] J. R. Melcher, Phys. Fluids **4**, 1348 (1961).
[27] A. L. Kupershtokh and D. A. Medvedev, Phys. Rev. E **74**, 021505 (2006).
[28] H. Hori, O. Urakawa, O. Yano, and Q. Tran-Cong-Miyata, Macromolecules **40**, 389 (2007).
[29] Z. Lin, T. Kerle, T. P. Russell, E. Schäffer, and U. Steiner, Macromolecules **35**, 3971 (2002).
[30] K. Amundson, E. Helfand, X. Quan, and S. D. Smith, Macromolecules **26**, 2698 (1993).
[31] G. Venugopal, S. Krause, and G. E. Wnek, Chem. Mater. **4**, 1334 (1992); G. Venugopal and S. Krause, Macromolecules **25**, 4626 (1992); K. Xi and S. Krause, *ibid.* **31**, 3974 (1998).
[32] T. Araki and H. Tanaka, J. Phys.: Condens. Matter **18**, L305 (2006).
[33] A. Onuki, Physica A **217**, 38 (1995).
[34] S. A. Madbouly, T. Chiba, T. Ougizawa, and T. Inoue, Polymer **42**, 1743 (2001).
[35] T. P. Russell, R. P. Hjelm, Jr., and P. A. Seeger, Macromolecules **23**, 890 (1990).
[36] M. Doi and H. See, *Introduction to Polymer Physics* (Oxford University Press, Oxford, 1996), p. 98.
[37] C. Redon, F. Brochard-Wyart, and F. Rondelez, Phys. Rev. Lett. **66**, 715 (1991).
[38] P. Lambooy, K. C. Phelan, O. Haugg, and G. Krausch, Phys. Rev. Lett. **76**, 1110 (1996).
[39] H. Tanaka, J. Phys.: Condens. Matter **13**, 4637 (2001).
[40] C. Wang, G. Krausch, and M. Geoghegan, Langmuir **17**, 6269 (2001).
[41] P. G. de Gennes, F. Brochard-Wyart, and D. Quere, *Capillarity and Wetting Phenomena: Drops, Bubbles, Pearls, Waves* (Springer, New York, 2003).
[42] I. M. de Schepper, H. E. Smorenburg, and E. G. D. Cohen, Phys. Rev. Lett. **70**, 2178 (1993); E. G. D. Cohen, R. Verberg, and I. M. de Schepper, Int. J. Multiphase Flow **23**, 797 (1997).
[43] B. Cichocki and B. U. Felderhof, J. Chem. Phys. **101**, 7850 (1994).
[44] S. Reich and J. M. Gordon, J. Polym. Sci., Polym. Phys. Ed. **17**, 371 (1979).
[45] J. S. Lee, A. A. Prabu, K. J. Kim, and C. Park, Macromolecules **41**, 3598 (2008).
[46] K. Orzechowski, Chem. Phys. **240**, 275 (1999).
[47] P. Debye and K. Kleboth, J. Chem. Phys. **42**, 3155 (1965).
[48] Y. Tsori, D. Andelman, C.-Y. Lin, and M. Schick, Macromolecules **39**, 289 (2006).